Direct Nanoscale Observations of CO$_2$ Sequestration during Brucite [Mg(OH)$_2$] Dissolution

J. Hövelmann,[†,*] C. V. Putnis,[‡] E. Ruiz-Agudo,[§] and H. Austrheim[†]

[†]Physics of Geological Processes, University of Oslo, 0316 Oslo, Norway
[‡]Institut für Mineralogie, University of Münster, 48149 Münster, Germany
[§]Department of Mineralogy and Petrology, University of Granada, 18071 Granada, Spain

Ⓢ *Supporting Information*

ABSTRACT: The dissolution and carbonation of brucite on (001) cleavage surfaces was investigated in a series of in situ and ex situ atomic force microscopy (AFM) experiments at varying pH (2−12), temperature (23−40 °C), aqueous NaHCO$_3$ concentration (10^{-5}−1 M), and PCO_2 (0−1 atm). Dissolution rates increased with decreasing pH and increasing NaHCO$_3$ concentration. Simultaneously with dissolution of brucite, the growth of a Mg−carbonate phase (probably dypingite) was directly observed. In NaHCO$_3$ solutions (pH 7.2−9.3,), precipitation of Mg−carbonates was limited. Enhanced precipitation was, however, observed in acidified NaHCO$_3$ solutions (pH 5, DIC ≈ 25.5 mM) and in solutions

that were equilibrated under a CO$_2$ atmosphere (pH 4, DIC ≈ 25.2 mM). Nucleation predominantly occurred in areas of high dissolution such as deep step edges suggesting that the carbonation reaction is locally diffusion-transport controlled. More extensive particle growth was also observed after ex situ experiments lasting for several hours. This AFM study contributes to an improved understanding of the mechanism of aqueous brucite carbonation at low temperature and pressure conditions and has implications for carbonation reactions in general.
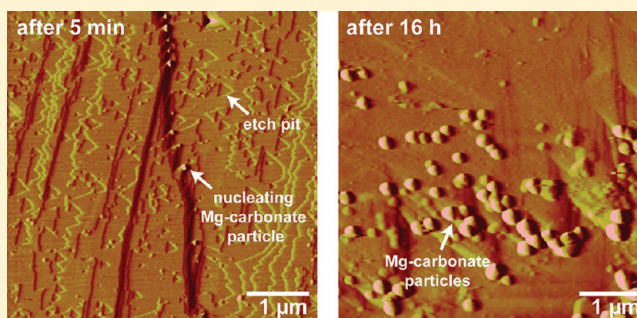
■ INTRODUCTION

Recently, many experimental studies have been devoted to the mineralization of CO$_2$, which is regarded as the safest and most permanent option for carbon sequestration.[1−8] So far, research has been focused on the carbonation of silicates such as olivine [(Mg,Fe)$_2$SiO$_4$] and serpentine [Mg$_3$Si$_2$O$_5$(OH)$_4$] because these minerals are available in vast quantities and thus represent the most promising feedstock materials for any ex situ mineral sequestration operation. Consequently, relatively few studies have dealt with the carbonation of brucite [Mg(OH)$_2$], a rather minor mineral in nature. Recently however, brucite is being given more interest, owing to its much higher reactivity relative to silicate minerals at low temperature and PCO_2 conditions.[9,10] Natural brucite is commonly formed in significant quantities (up to 20 wt %) during serpentinization of olivine-rich ultramafic rocks.[11] It is known that brucite is readily converted to hydrous magnesium carbonates such as hydromagnesite [Mg$_5$(CO$_3$)$_4$(OH)$_2$·4H$_2$O] or artinite [Mg$_2$(CO$_3$)(OH)$_2$·3H$_2$O] during weathering of serpentinite bodies.[11,12] The close association with serpentinites makes brucite also a common gangue mineral in ultramafic mine tailings. Hence, brucite carbonation may prove to be of practical significance to counterbalance the CO$_2$ emissions of some mining operations.[13,14] In the future, carbonation reactions involving brucite may gain even more attention since some researchers have recently started to develop magnesia cements that are

based on the hydration of MgO to form Mg(OH)$_2$.[15,16] MgO can be manufactured at lower temperatures than CaO and thus magnesia cements are thought to be more sustainable than conventional Portland cements. Furthermore, the CO$_2$ released during production of MgO can be reabsorbed when these cements carbonate. Utilization of brucite in any of the mentioned applications requires an in-depth understanding of the associated reaction mechanisms. Brucite dissolution rates have been studied in macroscopic batch and flow-through experiments as a function of pH, ionic strength, and solution saturation[17] as well as in the presence of various organic and inorganic ligands and divalent metals.[18] Macroscopic experiments on brucite carbonation have been performed in CO$_2$-bearing aqueous solutions[9] as well as in dry[19] and wet[10] supercritical CO$_2$. Zhao et al.[9] reported that aqueous carbonation of brucite is rapid at room temperature and moderate PCO_2 leading to almost complete conversion into nesquehonite (MgCO$_3$·3H$_2$O) within a few hours.

We have conducted a series of in situ and ex situ atomic force microscopy (AFM) experiments enabling direct nanoscale observations of dissolution and precipitation features on brucite

(001) cleavage surfaces. Although the dissolution behavior of brucite in acidic to neutral solutions has been investigated by AFM to some extent,[20,21] no previous AFM study that we know of has been concerned with brucite carbonation. Brucite is highly suitable for AFM experiments because a perfect (001) cleavage gives the possibility of almost atomically flat surfaces. Also, the relatively fast dissolution rates in the near-neutral pH region enable real-time observations. Its simple, layered structure is also a fundamental unit of many Mg-rich sheet silicates (e.g., serpentines and chlorite group minerals). Thus, studying the carbonation of brucite may also elucidate the mechanisms of mineral carbonation in a somewhat broader sense.

The AFM observations and measurements of the present study were made to characterize the coupling between brucite dissolution and carbonate precipitation on the nanoscale under a range of pH (2−12), temperature (23−40 °C), aqueous $NaHCO_3$ concentration (10^{-5}−1 M), and PCO_2 (0−1 atm). On the basis of our results, we identify potential implications for the technological development of brucite carbonation.

■ MATERIALS AND METHODS

All experiments were performed on natural brucite from the Tall Mine, an abandoned iron mine in a B-bearing iron formation located in the Norberg area of Bergslagen (Sweden). The specimen contained minor impurities of dolomite $[CaMg(CO_3)_2]$ and pyroaurite $[Mg_6Fe_2(CO_3)(OH)_{16}\cdot4H_2O]$, which were avoided for the AFM specimen preparation, where only optically transparent brucite crystals were used. Immediately before each experiment the crystals were cleaved in air with a razor blade along (001) planes to obtain fragments of ca. 3 × 3 × 0.2 mm. Before exposure to the experimental solution, doubly deionized water (resistivity >18 mΩ cm^{-1}) was passed over the crystal to clean the cleaved surface as well as to adjust the AFM operating parameters. Inorganic carbon was introduced into the reaction solutions in two ways: (1) by adding calculated amounts of $NaHCO_3$ or (2) by equilibrating deionized water under a CO_2 atmosphere. Adjustments of pH were done by adding a reagent grade acid (HCl or H_2SO_4) or base (NaOH). All experimental solutions were prepared immediately before use, except for those that were allowed to equilibrate with CO_2. Concentrations of total dissolved inorganic carbon (DIC) in the starting solutions were measured using an ion selective electrode. The chemical speciation of the solutions was determined using the PHREEQC computer program.[22] More details of the solution preparation, DIC measurements and speciation calculations can be found in the Supporting Information.

In situ AFM observations of the brucite (001) surface were performed in a fluid cell of a Digital Instruments Nanoscope III Multimode AFM working in contact mode at ambient temperature (23 ± 1 °C). At intervals of about 1.5 min before each scan, 1.5 mL solution were injected with a syringe giving an effective flow rate of approximately 60 mL h^{-1}. In some experiments, solutions were heated to 40 °C prior to injection to investigate the effect of increased temperature on brucite dissolution and carbonation. Images were taken every 1.5 min and the time automatically recorded. The scanned area was typically 5 × 5 or 10 × 10 μm. AFM images were collected using Si_3N_4 tips (Veeco Instruments, tip model NP-S20) with spring constants of 0.12 and 0.58 N m^{-1}. Quantitative analyses of AFM images were made using the NanoScope software (Version 5.12b48). Brucite dissolution typically results in the

formation of triangular etch pits with edges parallel to [100], [110] and [010].[21] Following Kudoh et al.[21] the etch pit spreading rate or retreat velocity v can be expressed by:

$$v = \frac{dx}{dt} \tag{1}$$

where x denotes the distance from the center of the triangle to the edge. By geometry, x is related to the edge length a of the triangle as:

$$x = \frac{1}{2\sqrt{3}}a \tag{2}$$

The combination of eqs 1 and 2 enables the calculation of v after measuring the increase of a per unit time in sequential AFM images. Values for v were obtained from the analysis of at least five etch pits in three pairs of sequential images of a given experimental run. In several experiments, scanning was stopped from time to time and the solution in the fluid cell was maintained static for several minutes up to a few hours, hence, allowing the system to approach equilibrium.

Ex situ AFM experiments were performed in the following way: freshly cleaved surfaces were mounted onto a sample holder and first observed by AFM in air and deionized water followed by a few scans in the experimental solution. The sample was then removed from the AFM and placed in a beaker filled with ∼25 mL of the reaction solution. The beaker was sealed with Parafilm and left overnight at either room temperature (23 °C) or 40 °C. On termination of an ex situ experiment, the sample was recovered from the solution, placed onto filter paper, and dried by putting a wick of filter paper carefully in contact with the upper surface to remove the adsorbed fluid film as quickly as possible and avoid precipitation upon evaporation. Finally, the reacted crystal surface was reexamined by AFM. Some crystals were also examined with a scanning electron microscope (SEM, JEOL JSM 6460 LV) equipped with an energy dispersive X-ray (EDX) detector for qualitative chemical analyses.

■ RESULTS AND DISCUSSION

Dissolution Features on Brucite (001) Cleavage Surfaces. Dissolution of brucite on (001) cleavage surfaces mainly proceeded by the formation and spreading of etch pits with equilateral triangular shapes (Figure 1). This etch pit morphology is typically observed during brucite dissolution and results from the 3-fold rotation axis normal to the (001) surface.[21] Shallow etch pits with depths of around 0.5 nm (i.e., close to 0.47 nm, the thickness of one unit-cell layer) formed randomly on the surface. Deep and coaxial triangular etch pits were also observed that mostly grouped along lines suggesting that they originated from dislocations intersecting at the surface. At pH 5, the estimated total etch pit density was in the order of 0.5−1 × 10^9 pits cm^{-2} with mostly shallow etch pits. At pH 3−4, the number of shallow etch pits increased markedly resulting in a total etch pit density of 4−6 × 10^9 pits cm^{-2}. After the complete removal of one $Mg(OH)_2$ layer, new etch pits formed and spread, resulting in a layer-by-layer dissolution (parts A−C of Figure 2). At pH 3−4, we also observed an enhanced formation of deep etch pits reaching depths of around 4 nm. At pH 2, these deep etch pits spread rapidly resulting in a rough surface topography (parts D−F of Figure 2). Brucite dissolution was also observed in the presence of $NaHCO_3$ and proceeded with the formation and spreading of
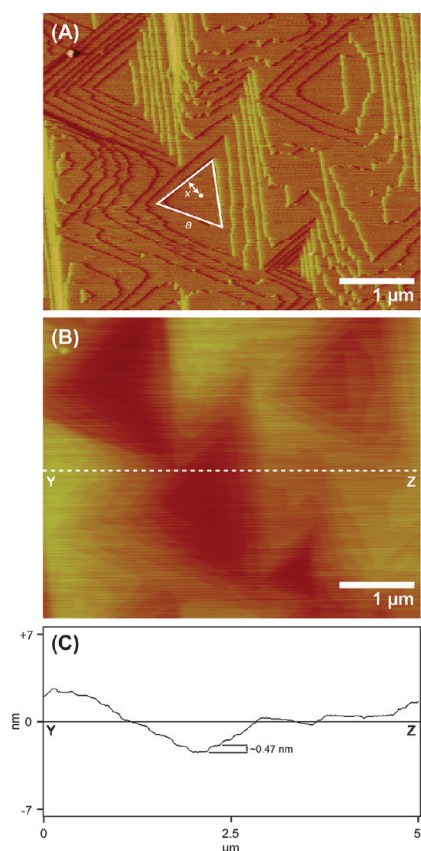
Figure 1. (A) AFM deflection and (B) height images of a brucite (001) surface showing the etch pit morphology developed after 2 h in contact with a pH 5.6 solution. Dissolution typically resulted in the evolution of etch pits with equilateral triangular shapes. The edge length a of individual etch pits was measured in sequential images to calculate the etch pit spreading rate (dx/dt) (text for details). (C) Depth profile showing the step height along section YZ (dashed line in (B)). The height of single steps is close to 0.47 nm corresponding to the thickness of one $Mg(OH)_2$ layer.

etch pits with the same characteristic triangular morphology (parts G–I of Figure 2).

The measured etch pit spreading rates (dx/dt) are shown as a function of pH in part A of Figure 3. In the circum-neutral pH region, the spreading rates ranged from 0.048 ± 0.012 nm s^{-1} at pH 8 to 0.071 ± 0.014 nm s^{-1} at pH 5. These values are 2–3 times higher compared to those reported by Kudoh et al.[21] for the same pH region. These authors adjusted the pH by using either a potassium hydrogen phthalate (for pH 5) or a sodium tetraborate (for pH 8) standard solution. However, in our AFM experiments the pH was adjusted by addition of HCl and NaOH, respectively. Hence, the observed discrepancy between the etch pit spreading rates obtained in the present study and the ones from Kudoh et al.[21] possibly indicates that phthalate and tetraborate (similar to other inorganic and organic ligands such as boric acid at neutral pH or acetate at alkaline pH[18]) have inhibitory effects on brucite dissolution.

In the acidic pH range, etch pit spreading rates rapidly increased with decreasing pH, from 0.22 ± 0.04 nm s^{-1} at pH 4 to 0.70 ± 0.07 nm s^{-1} at pH 2. Above pH 8, the etch pit retreat velocities quickly decreased from 0.030 ± 0.008 nm s^{-1} at pH 9 to virtually zero at pH 10–12, where etch pit spreading was not observed within 60 min of continuous solution flow. The increase of the etch pit retreat velocity with decreasing pH can

be explained by considering that the dissolution rate of brucite is a function of the $>MgOH_2^+$ surface concentration (where the notation > indicates an unbonded site).[17] Increasing H$^+$ activity results in enhanced protonation of $>MgOH^0$ surface sites leading to the formation of $>MgOH_2^+$, hence promoting brucite dissolution.

Etch pit spreading rates were also determined in the presence of 10^{-5}, 10^{-4}, 10^{-3}, 10^{-2}, 10^{-1}, and 1 M NaHCO$_3$ solutions with pH values ranging from 7.2 to 9.3 (part B of Figure 3). The results reveal a continuous increase in etch pit retreat velocity with increasing NaHCO$_3$ concentration, from 0.038 ± 0.004 nm s^{-1} at 10^{-5} M to 0.38 ± 0.07 nm s^{-1} at 1 M NaHCO$_3$. A comparison of these values with those measured in the absence of NaHCO$_3$ (part C of Figure 3) indicates that etch pit spreading is promoted by the addition of NaHCO$_3$. While no effect was observed at very low ($<10^{-3}$ M) NaHCO$_3$ concentrations, significantly increased etch pit retreat velocities were measured at all concentrations above 10^{-3} M. For example, the spreading rate measured in the presence of 1 M NaHCO$_3$ (pH 8.7) was about 1 order of magnitude higher compared to that in the pH 9 solution without added NaHCO$_3$. This observation is consistent with Pokrovsky et al.[18] who found that HCO$_3^-$ has a catalyzing effect on brucite dissolution due to the formation of multidentate mononuclear surface complexes that destabilize Mg–O bonds and water coordination of Mg-atoms at the surface.

Precipitation Features. Brucite dissolution in C-bearing solutions was accompanied simultaneously by nucleation and growth of a secondary phase on the brucite surface. In NaHCO$_3$ solutions (pH 7.2–9.3) secondary phase precipitation was limited. However, enhanced precipitation was observed in acidified NaHCO$_3$ solutions (pH 5, DIC ≈ 25.5 mM) as well as in solutions that were equilibrated with ca. 1 atm CO$_2$ (pH 4, DIC ≈ 25.2 mM). In addition, precipitation appeared to be promoted when the solution temperature was increased to 40 °C. The growth of the new phase was clearly related to the dissolution of the substrate such that conditions giving faster dissolution (lower pH, higher T) also accompanied faster precipitation. This means the growth was rate-limited by the release of Mg^{2+} ions. Nucleation of the new phase predominantly occurred in areas of enhanced dissolution such as deep step edges (parts A–D of Figure 4). A similar phenomenon has also been observed during epitaxial growth of brushite (CaHPO$_4$·2H$_2$O) onto gypsum (CaSO$_4$·2H$_2$O).[23] Initially, deep step edges were more or less straight, but when brucite started to dissolve, they tended to develop a sawtoothed morphology due to the coalescence of adjacent triangular etch pits (part B of Figure 4). The secondary phase preferentially nucleated at the tips of the saw-teeth. This can be understood if one considers that the Mg-atoms at the tips are coordinated to only 3 instead of otherwise 5 or 6 OH-groups (part E of Figure 4). Low coordination sites are more reactive than sites with higher coordination and hence, are expected to have a higher tendency to adsorb molecules or ions. In the early stage, nucleating particles were only 1–2 nm and weakly attached to the brucite surface as they could be easily pushed away by the scanning tip during in situ AFM experiments (part D of Figure 4). This may suggest that there is a low degree of epitaxial matching between the precipitating secondary phase and the brucite substrate. The movement of nucleated particles during scanning did not allow for a rigorous determination of nucleation and growth kinetics. Nevertheless, growth of the nucleated particles could be observed after keeping the fluid
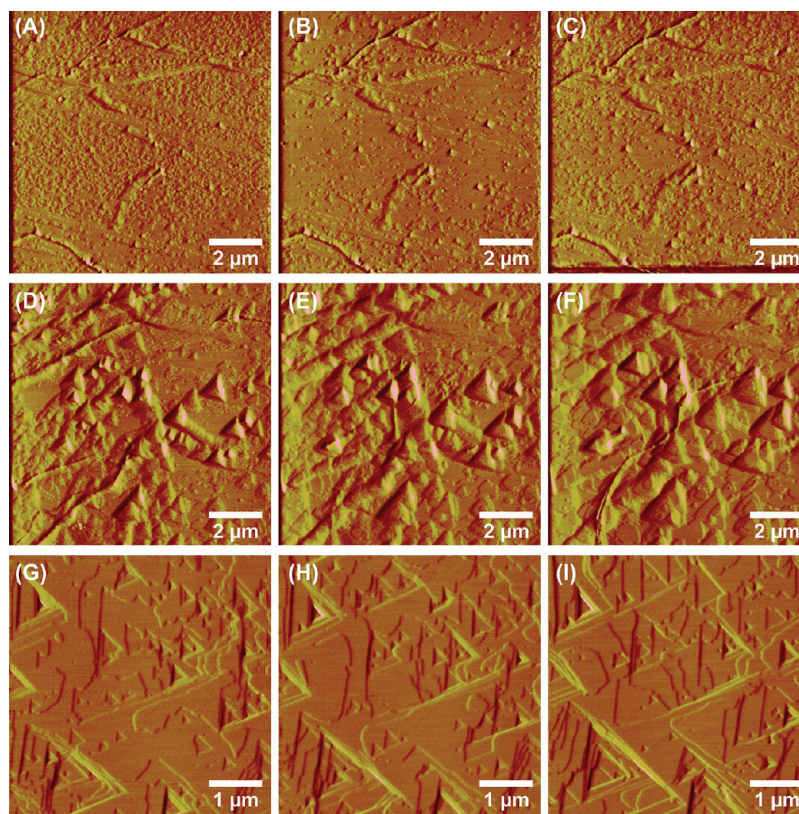
Figure 2. AFM time sequence (deflection images) of brucite dissolution in (**A–C**) deionized water + HCl (pH 4), (**D–F**) deionized water + HCl (pH 2), and (**G–I**) 1 M NaHCO$_3$ (pH 8.7). The images were taken at time intervals of about 2 min.
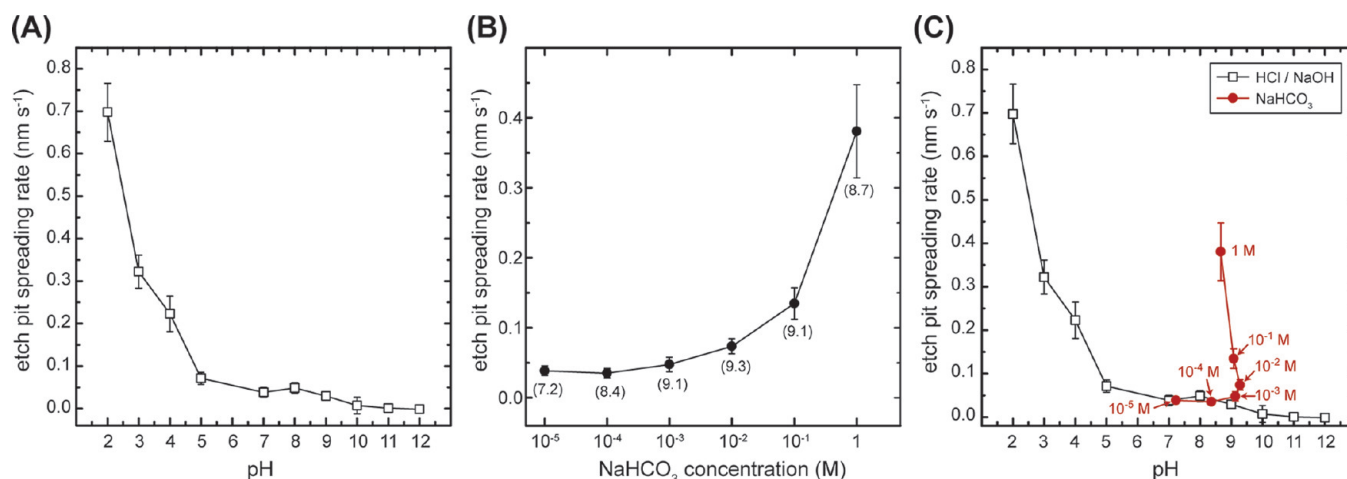

Figure 3. Etch pit spreading rates ($\mathrm{d}x/\mathrm{d}t$) as a function of (**A**) pH and (**B**) NaHCO$_3$ concentration. Bracketed numbers in (B) indicate the measured pH value of the corresponding solution. (**C**) Combined plot of (A) and (B). Error bars indicate the standard deviation of the measured values.

stagnant for a period. After 30 min, some particles had reached sizes of up to 10 nm (Figure 5). Further growth was observed after ex situ AFM experiments lasting for several hours (Figure 6). After 16 h, the size of individual particles was increased to about 100 nm. Some particles showed flat top surfaces indicating the formation of a crystalline phase (part C of Figure 6). Lateral spreading of the particles was rather limited, but instead we observed the formation of particle clusters reaching total heights of up to 1 μm after 32 h (part D of Figure 6). This observation points to a Volmer–Weber mechanism of epitaxial growth implying (1) a much higher adhesion of

subsequent growth on the secondary phase than on the brucite surface and (2) a large linear misfit between the two phases.[24] Consequently, the formation of high islands instead of a thin, continuous growth layer would be expected.

Precipitating Phase. AFM provides topographical information and does not allow for direct chemical determination of the precipitating phase. Therefore, ex situ techniques such as SEM, X-ray diffraction (XRD) or Raman spectroscopy had to be used in trying to better characterize the newly formed phase. After exposing freshly cleaved brucite surfaces to the C-bearing solutions for one day, precipitates were still too small to be
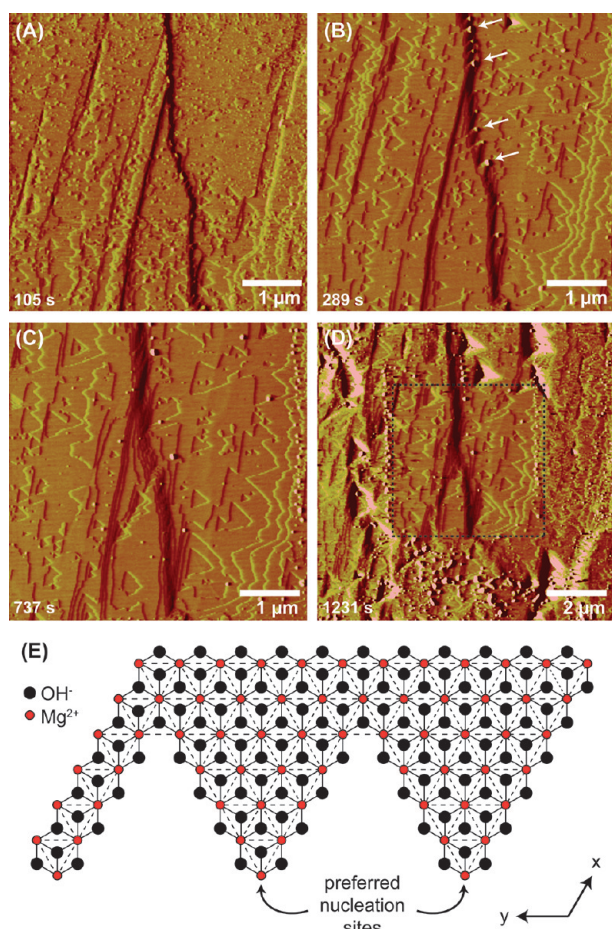
Figure 4. Sequence of AFM deflection images depicting brucite dissolution and secondary phase nucleation in an acidified $NaHCO_3$ solution (pH 5, DIC $\approx$ 25.5 mM). Reaction times are displayed on the lower left of each image. (**A**) Incipient dissolution around a deep, more or less straight step edge. (**B**) Development of a sawtoothed step edge morphology. Small particles nucleated at the tips of the saw-teeth (white arrows). (**C**) Nucleated particles were left behind upon further retreat of the step edge. Note that some small nuclei aligned at the right margin of the image indicating that they were pushed aside by the scanning tip. (**D**) Increased scan field (10 × 10 μm) showing that the scanning tip had cleared the former scan field (5 × 5 μm, indicated by the dashed rectangle) from smaller particles. (**E**) Structure of brucite projected on (001). The development of sawtoothed step edges during brucite dissolution produced surface sites, where Mg-atoms are coordinated to only 3 OH-groups. These sites were preferred for nucleation of the secondary phase.

visible in SEM. Sufficiently large particle clusters (part A of Figure 7) could however be produced in long-term ex situ experiments lasting for 7 days (Supporting Information for a detailed description). EDX analyses of these clusters revealed that they are composed of Mg, O, and C (part C of Figure 7). The underlying brucite possibly contributes to the Mg and O signals, however, the strong C signal that was not observed on unreacted surfaces indicates the presence of a Mg−carbonate. We were not able to unambiguously identify this phase by XRD or Raman spectroscopy, possibly because the amount of particle precipitates on individual brucite surfaces was too low. To increase the amount of reaction products, we performed experiments under the same conditions, but using 0.4 g of a fine-grained (<63 μm) brucite powder (Supporting Information of a detailed description). XRD analyses of the reacted
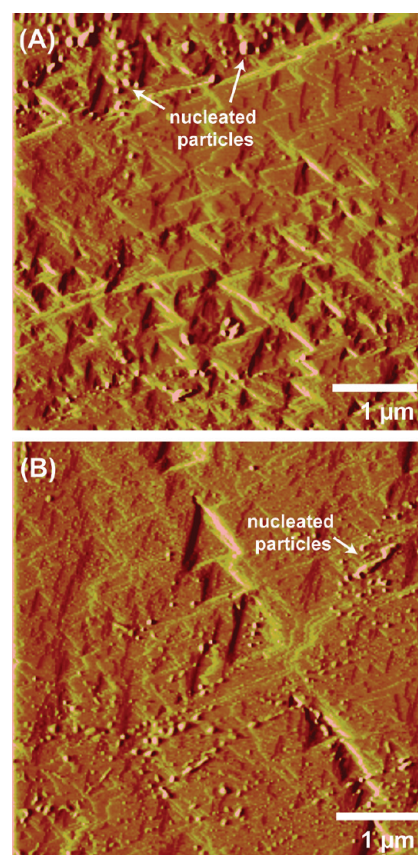

Figure 5. AFM deflection images showing the initial stages of brucite carbonation in deionized water equilibrated under a CO_2 atmosphere at 23 °C (pH 4, DIC $\approx$ 25.2 mM). Particles precipitated on the dissolving brucite surface are up to 10 nm in height. The images were taken after keeping the solution in the fluid cell stagnant for 30 min.

powders indicate the formation of dypingite $[Mg_5(CO_3)_4(OH)_2 \cdot \sim 5H_2O]$ (Figure S1 of the Supporting Information). Hence, we surmise that the phase that precipitated on the brucite surfaces during both ex situ and in situ AFM experiments is also dypingite. Dypingite is compositionally similar to hydromagnesite, but structurally more disordered with a variable amount of water molecules per formula unit.[25−27] PHREEQC modeling of brucite dissolution in the experimental solutions (Figure S2 of the Supporting Information) indicates that, upon equilibration with brucite, the solutions should be supersaturated with respect to magnesite, hydromagnesite, and artinite and close to saturation with respect to nesquehonite and lansfordite ($MgCO_3 \cdot 5H_2O$). The saturation state with respect to dypingite could not be calculated due to the lack of thermodynamic data for this phase. Magnesite, although being the thermodynamically most stable Mg−carbonate, is not expected to form at low temperatures due to a kinetic inhibition that is related to the strong hydration of Mg^{2+} ions in aqueous solutions.[28] Similarly, hydromagnesite precipitation may be kinetically impeded at temperatures below 40 °C.[29] At low temperatures, dypingite and nesquehonite are most commonly observed to form.[13,14,29−34] It is known that nesquehonite starts to precipitate at low supersaturation and that it may act as precursor for hydromagnesite or hydromagnesite-like phases such as dypingite.[26,32,35,36] Hence, it seems also possible that the first phase that nucleated under our in situ experimental conditions was nesquehonite, which was subsequently trans-
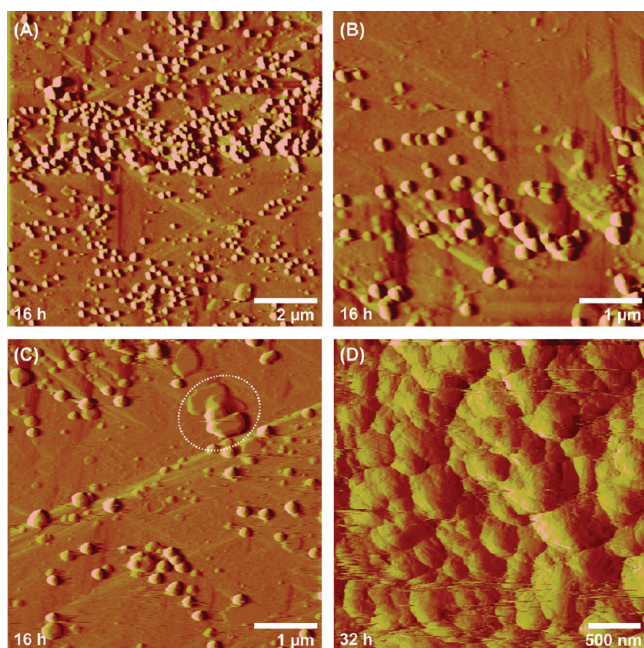
Figure 6. AFM deflection images showing precipitates formed on a brucite (001) surface during exposure to an acidified NaHCO$_3$ solution (pH 5, DIC ≈ 25.5 mM)) in ex situ experiments at 40 °C. (**A–C**) After 16 h: Numerous particles (mostly concentrated in clusters at larger steps) were formed on the brucite surface. Individual particles measure up to 100 nm in height. Note that some larger particles in (**C**), e.g., within the dotted circle, show flat surfaces indicative of a crystalline phase (**D**) After 32 h: large clusters of precipitates (up to 1 μm high) were formed on the brucite surface. The noise in the lower and upper part of the image is due to interference caused by the high surface roughness.

Figure 7. (**A**) SEM image of a brucite surface after 7 days of reaction in deionized water equilibrated under a CO$_2$ atmosphere (pH 4, DIC ≈ 25.2 mM) revealing larger clusters of a newly formed precipitate. (**B**) EDX spectrum taken from the brucite surface. The small C-peak is related to sample coating for imaging. (**C**) EDX spectrum taken from the precipitate. The markedly increased C-peak, together with the Mg-peak, indicates a Mg-rich carbonate phase.

formed into dypingite. It should also be noted that there are a number of other disordered precursor phases (including some poorly known unnamed phases[36]), which could possibly have played a role during our AFM experiments.

Role of the Interfacial Fluid Layer. Previous studies concluded that brucite dissolution is mostly surface-controlled in the pH range tested.[17,20,37] Assuming that both dissolution and precipitation are controlled by the >MgOH$_2$^+ surface species, our observations, that nucleating particles were more abundant at lower pH, would be consistent with a surface-controlled reaction. Nucleating particles were however also more abundant in areas of high topography, which represent areas of enhanced dissolution. This suggests that locally there is a significant contribution of diffusive transport to the control of the reaction. If the supply of new Mg^{2+} ions from the dissolving brucite surface is faster than the diffusion of dissolved Mg^{2+} ions from the solution-solid boundary into the bulk solution, a concentration gradient close to the brucite surface will develop. This could allow for the build-up of a Mg-concentration that is high enough to overcome a supersaturation threshold and induce nucleation of the new phase. Therefore, supersaturation with respect to the new phase may only be reached locally within a small fluid layer at the solution-solid boundary. Subsequent precipitation and diffusional exchange between the bulk solution and the interfacial fluid may then again result in an undersaturation of the fluid boundary layer with respect to the newly formed precipitate. Consequently, the new phase will continuously dissolve and reprecipitate during the experiment. A similar conclusion was made by Urosevic et al.,[38] who
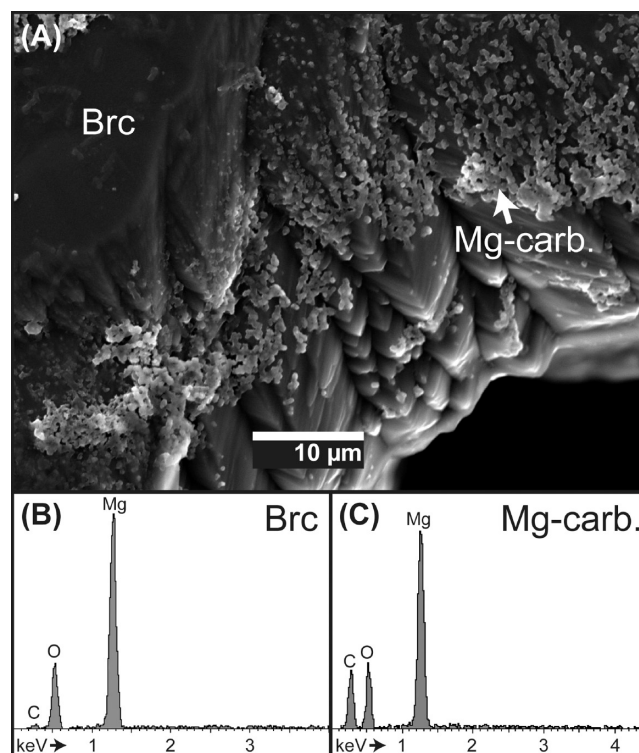
observed the precipitation of a Mg–carbonate on dissolving dolomite (10$\bar{1}$4) surfaces during in situ AFM experiments. Our results therefore emphasize the important role of the solution composition at the solid–fluid interface during mineral replacement reactions.[39,40]

Implications for CO$_2$ Sequestration. Our study indicates that brucite carbonation is rate-limited by the release of Mg^{2+} ions from the dissolving surface. The dissolution rate of brucite and hence the release of Mg^{2+} ions could be increased by decreasing the pH, adding catalytic ligands (e.g., HCO$_3$^-), or increasing the temperature. Higher temperatures not only accelerate brucite dissolution, but are also likely to increase the supersaturation with respect to hydrous Mg–carbonates, as these phases, like magnesite, exhibit retrograde solubility. Therefore, a rise in temperature could significantly enhance the efficiency of industrial brucite carbonation. A positive effect on carbonate precipitation could indeed be noticed as we increased the solution temperature to 40 °C.

During our AFM experiments, the brucite surfaces became increasingly covered by precipitates with time. This may finally lead to surface passivation reducing the carbonation potential. Thus, a large initial surface area is probably beneficial for industrial brucite carbonation. Surface passivation will, however, be dependent on whether or not interconnected porosity is generated within the precipitating layer. The generation of porosity in turn largely depends on the relative solubilities of the dissolving and the precipitating phases.[39] As the solubilities vary with temperature and solution composition, it seems reasonable that surface passivation is ultimately controlled by

these parameters. Nevertheless, the precipitates formed during our in situ AFM experiments were only weakly attached to the brucite surface. Stirring may therefore be an effective way to detach the precipitates from the brucite, hence reducing the risk of surface passivation.

◼ ASSOCIATED CONTENT

ⓢ Supporting Information

Further information of solution preparation, solution speciation, experimental procedures, and analytical methods as well as graphical representations of XRD and PHREEQC modeling results. This material is available free of charge via the Internet at http://pubs.acs.org.

◼ AUTHOR INFORMATION

Corresponding Author
*Phone: +47 22 85 60 48, fax: +47 22 85 51 01, e-mail: j.e. hovelmann@fys.uio.no.

Notes
The authors declare no competing financial interest.

◼ ACKNOWLEDGMENTS

◼ REFERENCES

(1) O'Connor, W. K.; Dahlin, D. C.; Rush, G. E.; Gerdemann, S. J.; Nilsen, D. N. *Final Report: Aqueous Mineral Carbonation*; Albany Research Center: Albany, OR, 2004.

(2) Giammar, D. E.; Bruant, R. G.; Peters, C. A. Forsterite dissolution and magnesite precipitation at conditions relevant for deep saline aquifer storage and sequestration of carbon dioxide. *Chem. Geol.* **2005**, *217* (3−4), 257−276.

(3) Béarat, H.; McKelvy, M. J.; Chizmeshya, A. V. G.; Gormley, D.; Nunez, R.; Carpenter, R. W.; Squires, K.; Wolf, G. H. Carbon sequestration via aqueous olivine mineral carbonation: role of passivating layer formation. *Environ. Sci. Technol.* **2006**, *40* (15), 4802−4808.

(4) Dufaud, F.; Martinez, I.; Shilobreeva, S. Experimental study of Mg-rich silicates carbonation at 400 and 500°C and 1 kbar. *Chem. Geol.* **2009**, *265* (1−2), 79−87.

(5) Daval, D.; Martinez, I.; Corvisier, J.; Findling, N.; Goffé, B.; Guyot, F. Carbonation of Ca-bearing silicates, the case of wollastonite: experimental investigations and kinetic modeling. *Chem. Geol.* **2009**, *265* (1−2), 63−78.

(6) Garcia, B.; Beaumont, V.; Perfetti, E.; Rouchon, V.; Blanchet, D.; Oger, P.; Dromart, G.; Huc, A. Y.; Haeseler, F. Experiments and geochemical modelling of CO₂ sequestration by olivine: potential, quantification. *Appl. Geochem.* **2010**, *25* (9), 1383−1396.

(7) King, H. E.; Plümper, O.; Putnis, A. Effect of secondary phase formation on the carbonation of olivine. *Environ. Sci. Technol.* **2010**, *44* (16), 6503−6509.

(8) Hövelmann, J.; Austrheim, H.; Beinlich, A.; Munz, I. A. Experimental study of the carbonation of partially serpentinized and weathered peridotites. *Geochim. Cosmochim. Acta* **2011**, *75* (22), 6760−6779.

(9) Zhao, L.; Sang, L.; Chen, J.; Ji, J.; Teng, H. H. Aqueous carbonation of natural brucite: relevance to CO₂ sequestration. *Environ. Sci. Technol.* **2010**, *44* (1), 406−411.

(10) Schaef, H. T.; Windisch, C. F.; McGrail, B. P.; Martin, P. F.; Rosso, K. M. Brucite [Mg(OH)₂] carbonation in wet supercritical CO₂: An in situ high pressure X-ray diffraction study. *Geochim. Cosmochim. Acta* **2011**, *75* (23), 7458−7471.

(11) Mumpton, F. A.; Thompson, C. S. Mineralogy and origin of the Coalinga asbestos deposit. *Clays Clay Miner.* **1975**, *23* (2), 131−143.

(12) Hostetler, P. B.; Coleman, R. G.; Mumpton, F. A. Brucite in alpine serpentinites. *Am. Mineral.* **1966**, *51* (1−2), 75−98.

(13) Wilson, S. A.; Barker, S. L. L.; Dipple, G. M.; Atudorei, V. Isotopic disequilibrium during uptake of atmospheric CO₂ into mine process waters: implications for CO₂ sequestration. *Environ. Sci. Technol.* **2010**, *44* (24), 9522−9529.

(14) Wilson, S. A.; Dipple, G. M.; Power, I. M.; Thom, J. M.; Anderson, R. G.; Raudsepp, M.; Gabites, J. E.; Southam, G. Carbon dioxide fixation within mine wastes of ultramafic-hosted ore deposits: examples from the Clinton Creek and Cassiar chrysotile deposits, Canada. *Econ. Geol.* **2009**, *104* (1), 95−112.

(15) Liska, M.; Al-Tabbaa, A. Performance of magnesia cements in pressed masonry units with natural aggregates: production parameters optimization. *Constr. Build. Mater.* **2008**, *22* (8), 1789−1797.

(16) De Silva, P.; Bucea, L.; Sirivivatnanon, V. Chemical, microstructural and strength development of calcium and magnesium carbonate binders. *Cem. Concr. Res.* **2009**, *39* (5), 460−465.

(17) Pokrovsky, O. S.; Schott, J. Experimental study of brucite dissolution and precipitation in aqueous solutions: surface speciation and chemical affinity control. *Geochim. Cosmochim. Acta* **2004**, *68* (1), 31−45.

(18) Pokrovsky, O. S.; Schott, J.; Castillo, A. Kinetics of brucite dissolution at 25°C in the presence of organic and inorganic ligands and divalent metals. *Geochim. Cosmochim. Acta* **2005**, *69* (4), 905−918.

(19) Béarat, H.; McKelvy, M. J.; Chizmeshya, A. V. G.; Sharma, R.; Carpenter, R. W. Magnesium hydroxide dehydroxylation/carbonation reaction processes: implications for carbon dioxide mineral sequestration. *J. Am. Ceram. Soc.* **2002**, *85* (4), 742−748.

(20) Jordan, G.; Rammensee, W. Dissolution rates and activation energy for dissolution of brucite (001): a new method based on the microtopography of crystal surfaces. *Geochim. Cosmochim. Acta* **1996**, *60* (24), 5055−5062.

(21) Kudoh, Y.; Kameda, J.; Kogure, T. Dissolution of brucite on the (001) surface at neutral pH: in situ atomic force microscopy observations. *Clays Clay Miner.* **2006**, *54* (5), 598−604.

(22) Parkhurst, D. L.; Appelo, C. A. J. *User's guide to PHREEQC (Version 2) −a computer program for speciation, batch-reaction, one-dimensional transport, and inverse geochemical calculations*; U.S. Geological Survey, Water Resources: Denver, CO, 1999; pp 99−4259.

(23) Pinto, A. J.; Ruiz-Agudo, E.; Putnis, C. V.; Putnis, A.; Jiménez, A.; Prieto, M. AFM study of the epitaxial growth of brushite (CaHPO₄·2H₂O) on gypsum cleavage surfaces. *Am. Mineral.* **2010**, *95* (11−12), 1747−1757.

(24) Chernov, A. A. *Modern Crystallography III: crystal growth*. Springer-Verlag: Berlin: Berlin, 1984; p 246.

(25) Raade, G. Dypingite, a new hydrous basic carbonate of magnesium, from Norway. *Am. Mineral.* **1970**, *55* (9−10), 1457−1465.

(26) Davies, P. J.; Bubela, B. Transformation of nesquehonite into hydromagnesite. *Chem. Geol.* **1973**, *12* (4), 289−300.

(27) Canterford, J. H.; Tsambourakis, G.; Lambert, B. Some observations on the properties of dypingite, Mg₅(CO₃)₄(OH)₂·5H₂O, and related minerals. *Mineral. Mag.* **1984**, *48* (348), 437−442.

(28) Sayles, F. L.; Fyfe, W. S. The crystallization of magnesite from aqueous solution. *Geochim. Cosmochim. Acta* **1973**, *37* (1), 87−99.

(29) Hänchen, M.; Prigiobbe, V.; Baciocchi, R.; Mazzotti, M. Precipitation in the Mg-carbonate system - effects of temperature and CO₂ pressure. *Chem. Eng. Sci.* **2008**, *63* (4), 1012−1028.

5259

dx.doi.org/10.1021/es300403n | *Environ. Sci. Technol.* 2012, 46, 5253−5260

(30) Ferrini, V.; De Vito, C.; Mignardi, S. Synthesis of nesquehonite by reaction of gaseous CO_2 with Mg chloride solution: its potential role in the sequestration of carbon dioxide. *J. Hazard. Mater.* **2009**, *168* (2−3), 832−837.

(31) Kloprogge, J. T.; Martens, W. N.; Nothdurft, L.; Duong, L. V.; Webb, G. E. Low temperature synthesis and characterization of nesquehonite. *J. Mater. Sci. Lett.* **2003**, *22* (11), 825−829.

(32) Mavromatis, V.; Pearce, C. R.; Shirokova, L. S.; Bundeleva, I. A.; Pokrovsky, O. S.; Benezeth, P.; Oelkers, E. H. Magnesium isotope fractionation during hydrous magnesium carbonate precipitation with and without cyanobacteria. *Geochim. Cosmochim. Acta* **2012**, *76*, 161−174.

(33) Power, I. M.; Wilson, S. A.; Thom, J. M.; Dipple, G. M.; Southam, G. Biologically induced mineralization of dypingite by cyanobacteria from an alkaline wetland near Atlin, British Columbia, Canada. *Geochem. T.* **2007**, *8*, 13.

(34) Botha, A.; Strydom, C. A. Preparation of a magnesium hydroxy carbonate from magnesium hydroxide. *Hydrometallurgy* **2001**, *62* (3), 175−183.

(35) Hopkinson, L.; Rutt, K.; Cressey, G. The transformation of nesquehonite to hydromagnesite in the system $CaO-MgO-H_2O-CO_2$: an experimental spectroscopic study. *J. Geol.* **2008**, *116* (4), 387−400.

(36) Hopkinson, L.; Kristova, P.; Rutt, K.; Cressey, G. Phase transitions in the system $MgO-CO_2-H_2O$ during CO_2 degassing of Mg-bearing solutions. *Geochim. Cosmochim. Acta* **2012**, *76*, 1−13.

(37) Vermilyea, D. A. The dissolution of MgO and $Mg(OH)_2$ in aqueous solutions. *J. Electrochem. Soc.* **1969**, *116* (9), 1179−1183.

(38) Urosevic, M.; Rodriguez-Navarro, C.; Putnis, C. V.; Cardell, C.; Putnis, A.; Ruiz-Agudo, E. In situ nanoscale observations of the dissolution of {10−1 4} dolomite cleavage surfaces. *Geochim. Cosmochim. Acta* **2012**, *80*, 1−13.

(39) Putnis, A.; Putnis, C. V. The mechanism of reequilibration of solids in the presence of a fluid phase. *J. Solid State Chem.* **2007**, *180* (5), 1783−1786.

(40) Putnis, C. V.; Tsukamoto, K.; Nishimura, Y. Direct observations of pseudomorphism: compositional and textural evolution at a fluid-solid interface. *Am. Mineral.* **2005**, *90* (11−12), 1909−1912.